Tiwari, D., Skidchenko, E., Bowers, J., Yakushev, M. V., Martin, R., & Fermin, D. (2017). Spectroscopic and electrical signatures of acceptor states in solution processed Cu2ZnSn(S,Se)4 solar cells. *Journal of Materials Chemistry C*, *5*(48), 12720-12727. https://doi.org/10.1039/C7TC03953K

Spectroscopic and Electrical Signatures of Acceptor States in Solution Processed $Cu_2ZnSn(S,Se)_4$ Solar Cells

Received 00th January 20xx,
Accepted 00th January 20xx

DOI: 10.1039/x0xx00000x

www.rsc.org/

Devendra Tiwari[a], Ekaterina Skidchenko[b], Jake W Bowers[c], Michael V Yakushev[b,d,e], Robert W Martin[b] and David J Fermin[a,*]

The nature and dynamics of acceptor states in solution-processed $Cu_2ZnSn(S,Se)_4$ (CZTSSe) thin films are investigated by variable temperature photoluminescence (PL) and electrical impedance spectroscopy. Highly pure I-4 phase CZTSSe with the composition $Cu_{1.6}ZnSn_{0.9}(S_{0.23}Se_{0.77})_4$ is synthesized by sequentially spin coating of dimethyl-formamide/isopropanol solutions containing metal salts and thiourea onto Mo coated glass, followed by annealing in Se atmosphere at 540 °C. As-annealed films are highly compact with a thickness of 1.3 μm and grain sizes above 800 nm, with a band gap of 1.18 eV. Photovoltaic devices of 0.25 cm² with the architecture glass/Mo/CZTSSe/CdS/i-ZnO/Al:ZnO demonstrate a power conversion efficiency reaching up to 5.7 % in the absence of an anti-reflective coating. Under AM1.5G illumination at 296 K, the best device shows 396 mV open-circuit voltage (V_{OC}), 27.8 mA/cm² short-circuit current (J_{SC}) and 52% fill factor (*FF*). The overall dispersion of these parameters is under 15 % for a total of 20 devices. In the near IR region, PL spectra are dominated by two broad and asymmetrical bands at 1.14 eV (PL1) and 0.95 eV (PL2) with characteristic power and temperature dependences. Analysis of the device electrical impedance spectra also reveal two electron acceptor states with the same activation energy to those observed by PL. This allows assigning PL1 as radiative recombination at localized copper vacancies (V_{Cu}), while PL2 is associated with Cu_{Zn} antisites, broadened by potential fluctuations (band tails). The impact of these states on device performance as well as other parameters such as barrier collection heights introduced by partial selenization of the back contact is discussed.

Introduction

Over the last 10 years, two new families of materials dominate research efforts towards low-cost sustainable photovoltaic technologies, namely organo-inorganic hybrid lead perovskite and inorganic kesterites.[1] Although perovskite laboratory-scale champion cell efficiencies have gone through an impressive improvement from 3.8 % to over 22% in the last 8 years,[2,3] long-term stability and technology scalability remain formidable challenges.[3,4] Inorganic kesterites, in which $Cu_2ZnSn(S,Se)_4$ or CZTSSe is the most prominent example, are widely considered as replacement of the more matured $Cu(In,Ga)Se_2$ (CIGS) technology which has reached cell efficiencies above 22%.[5] Slower improvements of CZTSSe cell efficiencies in comparison to perovskites cells can partly be explained in terms of the vastly superior research efforts on the latter as reflected by the number of publications.[6] In order to substantially improve kesterite cell performances, it is crucial to assess the nature and origin of recombination pathways.

CZTSSe solar cells featuring conversion efficiency above 10% have been fabricated using a variety of physical vapor deposition and non-vacuum deposition routes, demonstrating their synthetic flexibility.[7,8] Even though kesterites structurally resemble CIGS, there are significant differences in terms of processing chemistry as well as the nature of electronic and structural defects.[7,9–11] For instance, studies suggest that CZTSSe is significantly more susceptible to deep point defects and interfacial trap states than CIGS.[7,10–12] Computational studies have also predicted the presence of numerous point defects (vacancies and antisite) as well as the presence of secondary phases including binary and ternary sulphides (e.g. Cu_2SnS_3).[12] A variety of approaches have been reported to mitigate such structural defects, including the introduction of additives as recently exemplified in our previous report. [13]

In the present study, we establish a link between the chemical nature of defect sites in CZTSSe and how they manifest themselves in device properties by correlating the temperature dependences of photoluminescence and electrical impedance. CZTSSe thin-films are prepared by a solution based method followed by reactive annealing in the presence of Se. Quantitative structural and spectroscopic analysis confirmed the formation of a pure I-4 phase with a composition of $Cu_{1.6}ZnSn_{0.9}(S_{0.23}Se_{0.77})_4$. PL studies show two bands located at 1.14 eV (PL1) and 0.95 eV (PL2) with well-

[a] *School of Chemistry, University of Bristol, Bristol BS8 1TS, United Kingdom.*
[b] *Department of Physics, SUPA, Strathclyde University, Glasgow G4 0NG, United Kingdom.*
[c] *Centre for Renewable Energy Systems Technology (CREST), Wolfson School of Mechanical, Electrical and Manufacturing Engineering, Loughborough University, Loughborough LE11 3TU, United Kingdom.*
[d] *Institute of Metal Physics UB RAS, 620990, S. Kovalevskaya Street 18, Ekaterinburg, Russia*
[e] *Ural Federal University, Mira 19, 620002 Ekaterinburg, Russia*

† Electronic Supplementary Information (ESI) available:
This includes figures and tables showing Reitveld refinement on selective X-ray diffraction from CZTSSe, structural parameters, statistic of solar cell parameters, characteristic impedance spectrum and fitting, equivalent circuit, temperature dependent electrical parameters, and capacitance-voltage profile of a solar cell.This includes film characterization details, thermogravimetric analysis of precursor, schematic the refined crystal structure, typical impedance spectra of devices with trial circuits and temperature dependence of R_1, C_1, R_2 and C_2]. See DOI: 10.1039/x0xx00000x

defined power and temperature dependences. Quantitative analysis shows that these sites are associated with acceptor states, most likely Cu-vacancies (PL1) and Cu_{Zn} antisite clusters (PL2). Devices with the structure Mo/CZTSSe/CdS/i-ZnO/Al:ZnO, with power conversion efficiencies of up to 5.7% under AM 1.5G illumination, were investigated by electrical impedance spectroscopy. Analysis of the impedance responses allowed identifying two time constants with similar activation energies of the PL responses. These studies link PL (chemically sensitive information) and electrical (device sensitive) responses, providing a key step toward understanding power conversion losses in these devices.

Experimental procedure

CZTSSe Film deposition, device fabrication and measurements

CZTSSe films are deposited from a single solution precursor solution consisting of copper (II) chloride, zinc chloride, tin (II) chloride and thiourea dissolved in 1:1 solvent mixture of dimethyl formamide and isopropanol with a total metal concentration of 0.93 M. The precursor solution is spin-coated onto 5 x 5 cm^2 Mo coated glass substrates and heated to 300 ^oC on a hotplate in air. This cycle is repeated 4 times to achieve the final thickness. These films are annealed in Se atmosphere in a graphite box at 540 ^oC using a MTI-OTF1200X furnace. Differential scanning calorimetry data reported in our previous work demonstrated that CZTS crystalizes from a similar precursor formulation at 480 ^oC.[13] Several reports have also shown that highly crystalline materials can be obtained upon annealing in the range of 450 to 550 ^oC.[14] No blocking layers to prevent Na diffusion to CZTSSe or Se diffusion to Mo layer are employed. The annealed films are etched in 10 % aq. KCN solution for 30 seconds and subsequently introduced in a chemical bath maintained 70 ^oC consisting $CdSO_4$, thiourea and ammonium hydroxide for CdS buffer layer deposition, following a protocol reported previously.[15] i-ZnO and Al: ZnO transparent conducting oxide layer are deposited by RF-sputtering. No metal contact and anti-reflection coating is deposited in present case and Al:ZnO acts as the top contact. Cells with total area of 0.25 cm^2 are scribed mechanically. J-V characteristic of devices are measured under simulated AM1.5G from a class AAA solar simulator (Wacom, Japan) with integrated power output of 100 mW/cm^2 at 296 K. External quantum efficiency (EQE) of devices are measured using a Bentham TM 300 monochromator (Bentham instruments) and illumination from Xe and halogen sources. A calibrated Si photodiode is used as the reference for J-V and EQE measurements. Low temperature PL measurements are performed using a custom made setup comprising a 514.5 nm Ar ion laser as excitation source, closed cycle liquid He cryostat for temperature variation, 1 m focal length monochromator and a biased InGaAs photodetector for acquiring the spectrum. Low temperature impedance measurements are done in a modified Linkam HFS 600PB4 cooling stage and Solatron impedance analyzer in the frequency range of 1 Hz and 1 MHz with an AC potential modulation of 25 mV rms.

Absorber layer characterization

Thermally annealed films are analyzed by X-ray Diffraction (Bruker D8 Advance powder diffractometer with CuKα radiation; step size 0.02^o at room temperature ~23 ^oC) complemented by quantitative Rietveld analysis (using Fullprof suite) and Raman spectroscopy with Renishaw inVia spectrometer and excitation from 514 nm Spectra physics diode laser. Diffuse reflectance spectra of films are measured in integrated sphere attachment in Perkin Elmer lambda 900 spectrometer against $BaSO_4$ reference. Scanning electron microscopy for analysis of morphology and energy dispersive analysis of X-rays (EDAX) for composition of films is performed in a Jeol iT300 microscope fitted with 80 mm^2 Oxford X-max detector for EDAX.

Results and discussion

CZTSSe film structure and device characteristics

The overall composition obtained from site occupancies is $Cu_{1.6}ZnSn_{0.9}(S_{0.23}Se_{0.77})_4$, while other structural parameters such as atomic positions are included in the Supporting Information (**Table s1**). This Cu-deficient and Zn-rich composition is typical of CZTSSe employed in high-performance solar cells.[7] No secondary phases of CZTSSe, e.g. binary metal sulpho-selenide and ternary $Cu_2Sn(S,Se)_3$, are identified in the XRD analysis.

Figure 1a shows the characteristic X-ray diffractogram of CZTSSe films obtained by annealing the precursor film containing metal salts and thiourea on Mo-coated glass at 540 ^oC in the presence of Se. As described in the methods section, the molecular precursors were deposited by successive spin-coating steps. The peaks belonging to CZTSSe are indexed in black. Apart from the peaks due to CZTSSe, peaks linked to Mo and $Mo(S,Se)_2$ are observed as a result of partial chalcogenization of the Mo substrate during the annealing step.

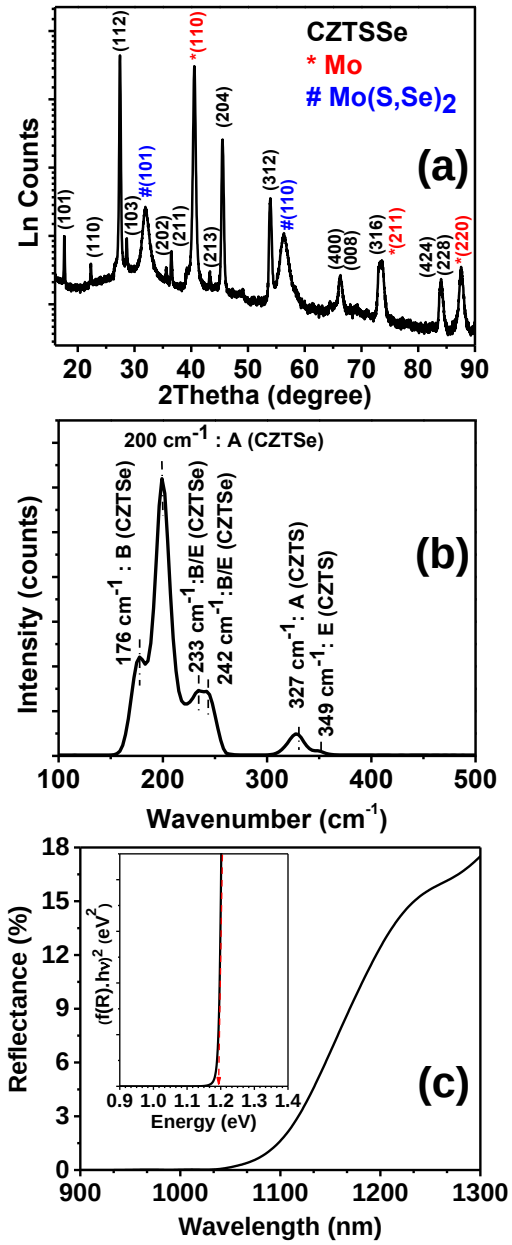

Figure 1. X-ray diffraction pattern (a) Raman spectrum under 514 nm excitation (b) and diffuse reflectance spectrum of as grown CZTSSe films (c). The inset in (c) shows a modified Tauc's plot using the Kubelka-Munk transformation of reflectance, resulting in an optical band gap of 1.18 eV. The structural and optical information are consistent with a I-4 phase with a composition $Cu_{1.6}ZnSn_{0.9}(S_{0.23}Se_{0.77})_4$.

To ascertain the phase purity of CZTSSe, Rietveld refinement of the peaks associated with the absorber was performed (Supporting Information, **Figure s1**).[16,17] The film crystallizes in kesterite phase (I-4) with unit cell parameters, a = 5.6494 (0.0014) Å and c = 11.2835 (0.003) Å. The overall composition obtained from site occupancies is $Cu_{1.6}ZnSn_{0.9}(S_{0.23}Se_{0.77})_4$, while other structural parameters such as atomic positions are included in the Supporting Information (**Table s1**). This Cu-deficient and Zn-rich composition is typical of CZTSSe employed in high-performance solar cells.[7] No secondary phases of CZTSSe, e.g. binary metal sulpho-selenide and ternary $Cu_2Sn(S,Se)_3$, are identified in the XRD analysis.

Further evidence of the film crystallographic phase is provided by the Raman spectrum shown in **Figure 1b**, measured under excitation at 514 nm. The spectrum shows two distinct regions pertaining to vibrational modes of CZTSe and CZTS. The first region, 150 to 260 cm^{-1}, has two sharp peaks at 176 and 200 cm^{-1} assigned to B and A symmetry modes of CZTSe in the kesterite phase, respectively. Two convoluted weak bands at 233 and 242 cm^{-1} are also observed, which are linked to B/E symmetry modes. The second region, 300 to 360 cm^{-1}, consists of two peaks at 327 and 349 cm^{-1} linked to A and E symmetry modes of CZTS, respectively. The peaks associated with the CTZSe and CZTS phases are blue and red shifted, respectively, in comparison to the Raman mode of the pure kesterites. (for eg. A mode: CZTS 338 cm^{-1} and CZTSe: 196 cm^{-1}). Furthermore, these results are consistent with literature for the sulphoselenide unit cell with a [Se]/[S] ~ 3, in agreement with the XRD analysis.[18]

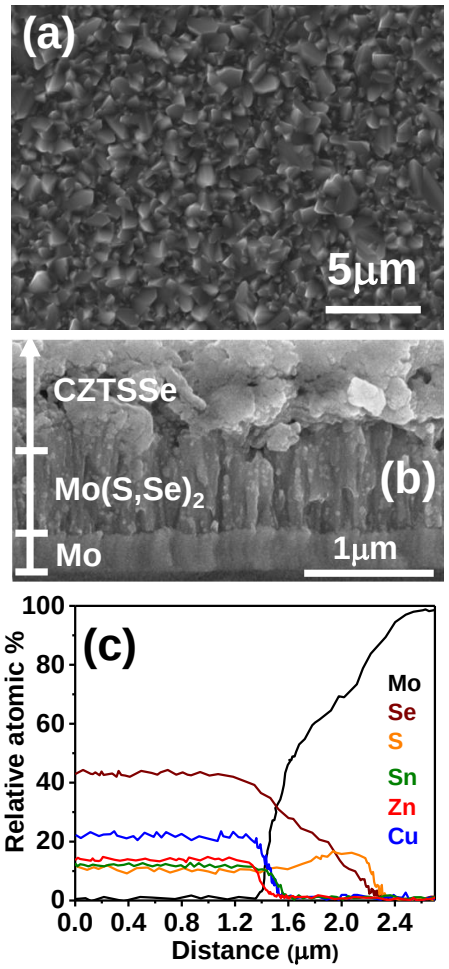

Figure 2. Top (a) and cross-sectional (b) scanning electron micrographs of annealed CZTSSe film. Composition profile using EDAX linescan across the CZTSSe/Mo film stack (c).

The diffuse reflectance spectrum in **Figure 1c** shows a sharp onset close to 1170 nm characteristic of a direct band-to-band transition. The Kubelka-Munk function as a function of incident photon energy (**inset Figure 1c**) is consistent with a direct band gap transition at 1.18 eV, which is also consistent with the degree of selenization obtained from XRD and Raman data.[19]

The SEM image in **Figure 2a** shows a homogenous and compact polycrystalline film after annealing, featuring grain sizes from 800 to 1400 nm. The cross-sectional SEM image in **Figure 2b** allows identifying three regions: (i) 1.3 μm thick top CZTSSe layer, (ii) 200 nm thick Mo layer at the bottom of stack and a (iii) 750 nm intermediate layer generated by the partial conversion of Mo to $Mo(S,Se)_2$. The elemental dispersive analysis of X-rays (EDAX) linescan in Figure 2c clearly shows that the Se and S signals extend beyond those of Cu, Zn and Sn, overlapping with the signal, confirming the presence of a $Mo(S,Se)_2$ layer. Se appears more prominent at the boundary between CZTSSe/$Mo(S,Se)_2$, while a slight S excess in observed at $Mo(S,Se)_2$/Mo junction. This trend suggests that MoS_2 is initially generated given that sulfur is already present in the molecular precursor, while Se has to diffuse through the film during annealing. Within the CZTSSe layer, the ratios of [Zn]/[Sn], [Cu]/([Zn]+[Sn]) and [Se]/[S] are 1.11, 0.82, and 2.8, respectively. The overall EDAX composition is consistent with the values estimated from XRD, Raman and band gap onset.

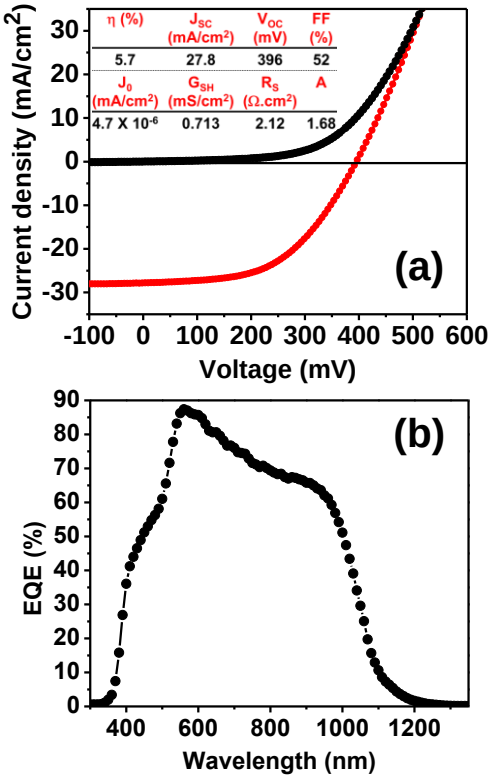

Figure 3. J-V characteristics under 100 mW/cm2 AM1.5G (a) and external quantum efficiency spectrum (b) of a 0.25 cm^2 device with the structure: glass/Mo/CZTSSe/CdS/i-ZnO/Al:ZnO The reverse saturation current (J_0), shunt conductance (G_{SH}), series resistance (R_S) and diode factor (A) derived *from the J-V under illumination are provided as inset to Figure 3a.*

Current-voltage (*J-V*) and external quantum efficiency spectra of devices with structure glass/Mo/CZTSSe/CdS/i-ZnO/Al:ZnO are displayed in **Figure 3**, in the absence of top metal contacts or anti-reflecting coating. The total area of the individual cells is 0.25 cm^2, defined by mechanically scribing. **Figure 3a** illustrates the *J-V* characteristics of the best cell in the dark and under simulated AM1.5G illumination, featuring a power conversion efficiency of 5.7%. The open-circuit voltage (V_{OC}), short-circuit current (J_{SC}) and fill factor (*FF*) estimated for this cell are 396 mV, 27.8 mA/cm^2 and 52%, respectively. The mean performance values for 20 devices are summarized in **Table s2**, showing a maximum deviation of less than 15%.

Figure 3b displays the external quantum efficiency (EQE) spectrum, showing a maximum value close to 90% at 2.21 eV. Estimation of the band-gap from the first derivative of the EQE spectrum with respect to photon energy yields a value of 1.17 eV, while a similar value was obtained from the intercept of $(h\nu(-Ln(1-EQE)))^2$ versus $h\nu$. This band-gap is consistent with the analysis of the diffuse-reflectance data (**Figure 2c**). Integrating the EQE spectrum with respect to AM1.5G results in a value of 27.6 mA/cm^2, consistent with the J_{SC} value in **Figure 3a**.

As commonly observed in these systems, the major limiting factor in device performance is linked to the V_{OC} deficiency and the low *FF*. For comparison, the 12.6% champion cell reported by IBM show V_{OC} and *FF* values of 466 mV and 69.8 %, respectively.[8] Interfacial and bulk recombination processes are the source of this limiting effect and the rest of the discussion will focus on the latter.

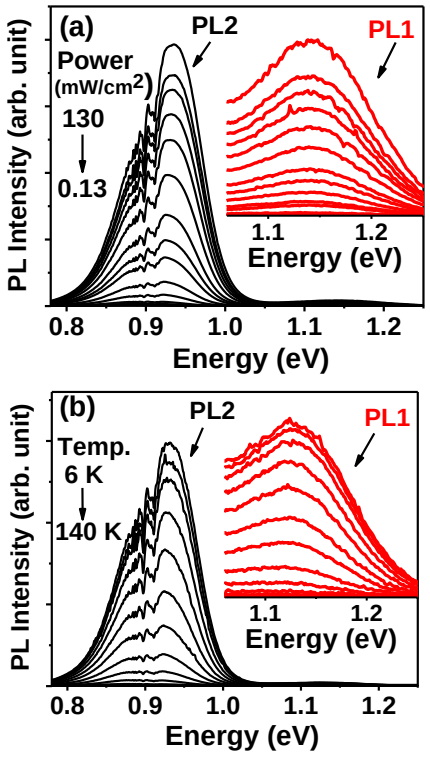

Figure 4. Photoluminescence spectra of CZTSSe films as a function of excitation power (a) and temperature (b). Insets expand on the region associated with PL1.

Carrier recombination Mechanisms based on photoluminescence measurements

The photoluminescence (PL) spectra of CZTSSe films measured as functions of excitation power and temperature are shown in **Figure 4 a** and **b**.

Two key features are observed, a weak band at 1.14 eV (PL1) and a stronger response at 0.95 eV (PL2). Both bands are found to be asymmetrical in shape, which is characteristic of heavily doped and compensated semiconductors including kesterites.[20–27] As discussed further below, the position of the bands is slightly affected by temperature and power intensity. Signals associated with water absorption around 0.9 eV introduce some interference in the analysis of the PL2 band, becoming a lot more significant at higher temperatures and lower excitation power.

In order to establish quantitative trends of PL1 and PL2 with respect to excitation intensity and temperature, each of them were fitted to a double sigmoidal function proposed by Krustok et al.[28], which considers asymmetry introduced by phenomena such as band tailing. **Figure 5a** shows that the maximum (E^*_{PL}) of the PL1 and PL2 bands is shifted to higher energies by approximately 6.5 meV per decade of incident power excitation. In a first approximation, this behavior can be rationalized in terms of the so-called donor-acceptor pair (DAP) recombination mechanism,[20]

$$E^*_{PL} = E_g - (E_A + E_D) + \frac{e^2}{4\pi\epsilon\epsilon_0 R^2} \approx E_g - (E_A + E_D) + 13.6 \times m^*/\varepsilon^2 \quad (1)$$

where E_g, E_A, E_D are the band gap, energies of acceptor and donor states, ε is the dielectric constant (for $Cu_2ZnSn(S_{0.2}Se_{0.8})_4$ = 8.8), ε_o = is permittivity of the free space, R is the shallow impurity Bohr radius and m^* is the electron effective mass. The last term in Eq. 1 represents the Coulombic interaction between the donor and the acceptor in the pairs, which corresponds to a value of approximately 17 meV for CZTSSe. From the analysis of Zacks and Halperin,[29] the shift expected by this model cannot be greater than 3 meV per decade of incident power, which is significantly lower than the experimental shifts shown in **Figure 5a**. Based on the fact that the width and shape of the peaks are only slightly affected by the excitation power, we conclude that the observed E_{PL} shifts involve not only contributions from DA repulsion, but also from filling of tail states. These tail states are linked to spatial potential fluctuations of band edges originating from inhomogeneous distribution of charged defect clusters. [20–23,25]

The variation of integrated peak intensity with excitation power is shown in **Figure 5b**, revealing a power dependence with exponent values (k) of 1.27 ± 0.02 and 0.74± 0.04 for PL2 and PL1 bands, respectively. The k value of PL1 is consistent with defect mediated recombination involving localized (trapped) carriers. On the other hand, the behavior of PL2 can be linked to recombination via charge carriers not localized on the defect level, and previous studies have reported k values as large as 1.7 in chalcopyrites and kesterites.[21–23] It is also noticeable that the peak position of PL1 has a stronger dependence on temperature than PL2 as shown in **Figure 5c**. This is further evidence that PL1 involves valence band tail states which effectively become acceptor states at low temperature.[23]

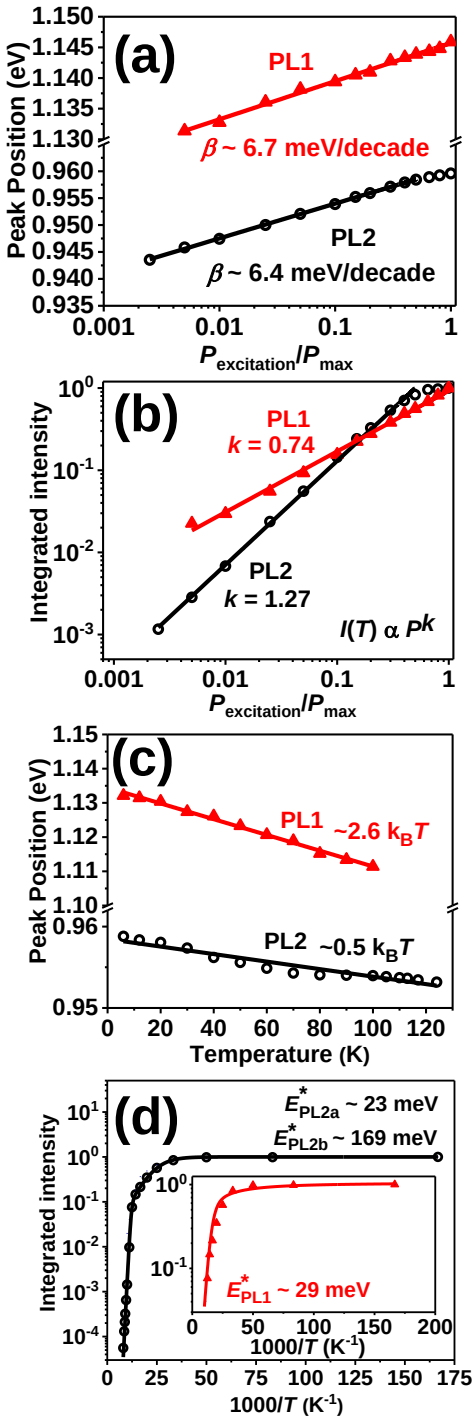

Figure 5. Excitation laser power dependence of the PL peak position (a) and integrated intensity (b). Temperature dependence of the PL peak positions (c) and integrated intensity (d). PL1 is characterized by a single activation energy, while PL2 showed two values depending on the temperature range.

Further valuable information on the nature of PL1 can be gained from the temperature dependence of the peak intensity as shown in **Figure 5d.** Thermal PL quenching can be described from a single radiative recombination channel, assuming temperature dependence of the hole capture cross section,[28]

$$I(T) = \frac{I_0}{1+\alpha_1 T^{3/2}+\alpha_2 T^{3/2}.Exp\left(\frac{-E^*_{PL1}}{k_B T}\right)} \quad (2)$$

where, I_o is the maximum intensity measured at 6 K, α_1 and α_2 are kinetic terms and E^*_{PL1} is the activation energy of the process. Fitting the data to Eq. 2 provides an activation energy of 29 meV. This value is comparable to the average depth of potential fluctuations (γ), which are responsible for broadening of PL responses,[20]

$$I \propto Exp\left[-\left(\frac{(E-E_o)^2}{2\gamma^2}\right)\right] \quad (3)$$

where, E_o is the peak maximum. From PL1 spectral broadening, γ is estimated to be 26 meV, which is in agreement with previous reports for similar CZTSSe composition.[27] The similarity between E^*_{PL1} and γ provides strong evidence that this spectral signature is dominated by a band to band-tail transition.[20,23,24,26,27] For the specific case of CZTSSe (with $m^*_h > m^*_e$), PL1 is most likely to be linked to a shallow acceptor state such as copper vacancies (V_{Cu}).[12]

The position and weak temperature dependence of PL2 (**Figure 5c**) excludes the possibility of involvement of valence band tails states or DAP recombination (large β value). Thus, the origin of PL2 can be assigned to a transition between the conduction band and a deep acceptor impurity level. The strong dependence of the PL2 peak intensity with temperature (**Figure 5d**) is characterized by a complex Arrhenius behavior with two activation energies,[25]

$$I(T) = \frac{I_0}{1 + c_1 Exp\left(\frac{-E^*_{PL2a}}{k_B T}\right) + c_2.Exp\left(\frac{-E^*_{PL2b}}{k_B T}\right)} \quad (4)$$

where, c_1 and c_2 are dimensionless parameters and E^*_{PL2a} and E^*_{PL2b} are the activation energy terms. E^*_{PL2a} is found to be 23 meV and E^*_{PL2b} is 169 meV. Again, E^*_{PL2a} is very close to the average depth of potential fluctuations in the conduction band edge. E^*_{PL2b} is linked to a deep acceptor level, which could be assigned to Cu_{Zn} antisites on the basis of first-principle calculations.[12] Indeed, even if the overall composition of the film is Cu poor and Zn rich, strong justification of Cu_{Zn} antisites have been obtained from neutron scattering studies and first principles calculation. [30–32] Zn_{Sn} antisites may also generate acceptors states located within the energy range observed,[12] however, very few reports have provided evidences of the presence of these states. Other types of defects are expected to generate significantly deeper or highly charged states.

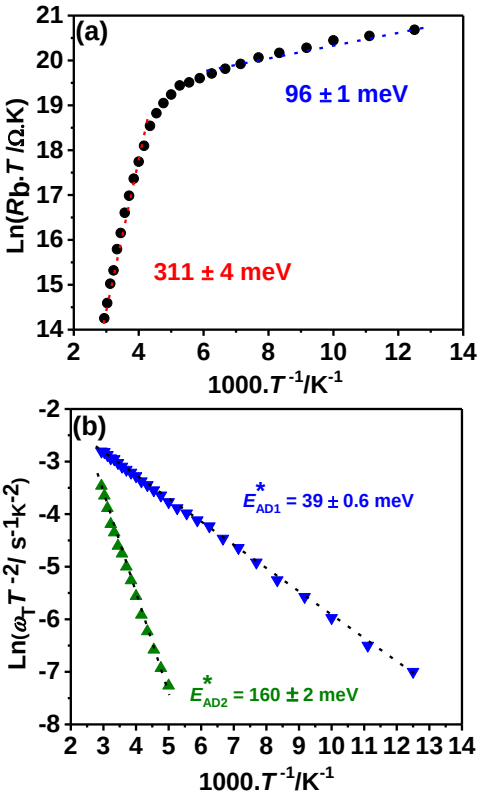

Figure 6. Temperature dependence of the back contact, revealing two barrier heights of 311 ± 4 meV and 96 ± 1 meV at high and low temperatures, respectively (a). These back contact barriers heights can be linked to transport across the CZTSSe/Mo(S,Se)$_2$/Mo double-junction. Temperature dependence of the relaxation frequencies of the two acceptor levels (b). The activation energies E^*_{AD1} and E^*_{AD2} closely correlate with the activation energies of EPL1 and EPL2, respectively.

Temperature dependence of the device electrical impedance

Impedance spectra of devices recorded up to 1 MHz and between 80 to 340 K are exemplified in **Figure s2a**. **Figure s2b** shows the equivalent circuit used in the impedance analysis, featuring two *RC* time constants associated with the CZTSSe/CdS (R_jC_j) and Mo(S,Se)$_2$/CZTSSe (R_bC_b) junctions, as well as two additional time constants (R_1C_1 and R_2C_2) linked to trap states in parallel.[15,33–36] The temperature dependences of the various resistance and capacitance elements are illustrated in **Figure s2c-e**. **Figure s2c** shows the decrease of the CZTSSe/CdS junction capacitance (C_j) with decreasing temperature down to a value of 1.55 nF. This geometric limit corresponds to a dielectric thickness of 1.35 μm, which closely agree with the film thickness measured by SEM. Furthermore, we have performed capacitance-voltage profiling as shown in **Figure s3,** following established methodologies.[37] The analysis provided a depletion width and doping density at zero bias of 175 nm and 1.6 x 10^{16} cm^{-3}, respectively.

Figure 6a shows the temperature dependence of the back-contact resistance (R_b), revealing two carrier collection barrier heights of 311 ± 4 meV and 96 ± 1 meV. This complex back contact behavior has been reported in previous studies,[34,36] and can be tentatively linked to the CZTSSe/Mo(S,Se)$_2$/Mo double junction. The large barrier height observed at high

temperatures have a strong detrimental effect in device performance, particularly on *FF*. Recent studies have shown a substantial increase in device performance after mechanically detaching the cell from the Mo film and attaching a fresh back contact.[38]

The temperature dependence of the trap states ($\omega_T = 1/RC$) are characterized by an Arrhenius type of behavior as shown in **Figure 6b,**[15,33–36]:

$$\omega_T = \xi_0 T^2 . \exp\left(\frac{E^*_{AD}}{k_B T}\right) \quad (5)$$

where, ξ_0 is the thermal emission factor and E^*_{AD} is the activation energy of the corresponding defect. The data in **Figure 5b** show activation energies E^*_{AD1}= 39 ± 0.6 and E^*_{AD2} = 160 ± 2 meV, respectively. There is a remarkable correlation between E^*_{AD1} and E^*_{PL1} as well as E^*_{AD2} and E^*_{PL2b} providing a direct link between the nature of acceptor states from electrical and optical responses.

Figure 7 illustrates the main finding of the combined spectroscopic and impedance studies, highlighting:

i. Band edges affected by potential fluctuations with an average depth $\gamma \approx 25$ meV

ii. Shallow acceptor states, assigned to V_{Cu}, located 30 meV above the valence band edge with an electron capture time constant (R_1C_1) of the order of 100 μs

iii. Deeper acceptor states, linked to Cu_{Zn} antisite clusters, located at 160 meV above the valence band edge with a time constant of 500 μs at room temperature.

V_{Cu} is the acceptor state with the lowest formation energy in Cu based chalcogenides such as CIGS and CZTSSe, resulting in the characteristic p-type conductivity of these materials.[9] It should be mentioned that DFT calculations are mainly performed in the dilute regime, i.e. assuming isolated (point) defects. However, the charge compensated nature of these materials suggests a high probability of defect clustering which are responsible for the potential fluctuation of the band edges (tail states). These tail states as well as deep traps introduced by Cu_{Zn} antisites are closely linked to bulk recombination and the loss of V_{OC}. Indeed, Monte-Carlo simulations considering the ensemble of defects have predicted potential fluctuations similar to the one obtained in our analysis.[11,39]

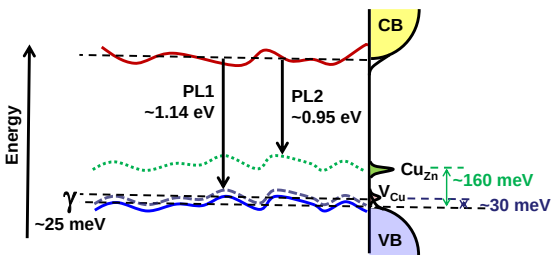

Figure 7. Schematic one dimension illustration of the band gap, showing tail states and the position of carrier capture by the acceptor states at room temperature.

We recognize that important contributions to the observation of Cu_{Zn} antisite defects have been made on the basis of order parameters estimated from crystallographic analysis[40] and Raman features,[41] however linking these parameters to specific recombination pathways and device efficiency in a quantitative manner remains a formidable challenge. If our key assignments are correct, this is a step forward in this direction. However, in order to establish a complete picture linking recombination kinetics and efficiency losses, additional information such as time resolved PL measurements are required as well as techniques capable of probing deeper states in the band gap, such as deep level transient spectroscopy (DLTS).[42] Indeed, Sn anti-sites are expected to generate mid-gap states, which may also have a significant contribution to device performance.[13,36,43] Finally charge compensation will arise from defect states located close to the conduction band, most probably connected to Zn_{Cu} antisite clusters.[12] Establishing spectroscopic and electrical signatures of these parameters are crucial in order to fully comprehend the recombination processes limiting the performance of the devices.

Conclusions

Our studies provide a clear link between spectroscopic and electrical signatures of trap states in CZTSSe films obtained by solution processing of molecular precursors and reactive annealing in the presence of Se. Quantitative XRD, Raman and diffuse reflectance spectroscopy and EDAX reveal highly pure I-4 phase with a stoichiometry $Cu_{1.6}ZnSn_{0.9}(S_{0.23}Se_{0.77})_4$ and a band gap of 1.18 eV. Devices with the structure Mo/CZTSSe/CdS/i-ZnO/AZO were fabricated with a total area of 0.25 cm^2, with no top metal contact or antireflective coating. The best cell performance provided a V_{OC}, J_{SC} *FF* of 396 mV, 27.8 mA/cm^2 and 52%, respectively, corresponding to a power conversion efficiency of 5.7%. Quantitative analysis of variable temperature PL and impedance spectroscopy allowed identifying two key acceptor states located at 160 and 30 meV from the valence band edge. The deeper state is characterized by a broad and asymmetric PL band (PL2), featuring two activation barriers as a function of temperature. We rationalize this observation in terms of emission from tail states in the conduction band (linked to potential fluctuations with an average depth of 23 meV) to an acceptor state assigned to Cu_{Zn} antisite. On the other hand, PL1 involves charge localized in an acceptor state assigned to V_{Cu}. Impedance spectroscopy of complete devices exhibited two time-constants associated with states featuring the same activation energy obtained from the PL spectra. This important correlation enables not only to confirm the acceptor nature of the states, but also provides valuable information with regards to the kinetics of charge trapping. These observations are crucially important for several reasons: (1) direct link between bulk spectroscopic features of the absorber layer and device electrical properties, (2) correlation between electron trapping and parameters such as the average band edge potential fluctuation, which is related to material disorder.

Conflicts of interest

There are no conflicts to declare

Acknowledgements

DT and DJF are indebted to the Engineering and Physical Sciences Research Council (EPSRC) funded PVTEAM grant (EP/L017792/1). DJF acknowledges Institute of Advanced Studies of the University of Bristol support as University Research Fellowship 2016. Impedance analysis is performed with Solartron analyzer procured under EPSRC CDT Capital grant EP/K035746/1. Microscopic imaging and analysis are done at the Chemical Imaging Facility, University of Bristol, with equipment funded by EPSRC Grant "Atoms to Applications" (EP/K035746/1). The authors are grateful to measurement facilities provided at CREST, Loughborough University and Department of Physics, SUPA, Strathclyde University.

Notes and references

‡ Further details of the crystal structure investigation(s) may be obtained from the Fachinformationszentrum Karlsruhe, 76344 Eggenstein-Leopoldshafen (Germany), on quoting the depository number CSD- 433445.

1 V. Steinmann, R. E. Brandt and T. Buonassisi, *Nat. Photonics*, 2015, **9**, 355–357.

2 J.-P. Correa-Baena, A. Abate, M. Saliba, W. Tress, T. Jesper Jacobsson, M. Grätzel and A. Hagfeldt, *Energy Environ. Sci.*, 2017, **10**, 710–727.

3 J. S. Manser, M. I. Saidaminov, J. A. Christians, O. M. Bakr and P. V. Kamat, *Acc. Chem. Res.*, 2016, **49**, 330–338.

4 E. Tenuta, C. Zheng and O. Rubel, *Sci. Rep.*, 2016, **6**, 37654-1–8.

5 P. Jackson, R. Wuerz, D. Hariskos, E. Lotter, W. Witte and M. Powalla, *Phys. Status Solidi - Rapid Res. Lett.*, 2016, **10**, 583–586.

6 S. K. Wallace, D. B. Mitzi and A. Walsh, *ACS Energy Lett.*, 2017, **2**, 776–779.

7 X. Liu, Y. Feng, H. Cui, F. Liu, X. Hao, G. Conibeer, D. B. Mitzi and M. Green, *Prog. Photovoltaics Res. Appl.*, 2016, **24**, 879–898.

8 J. Kim, H. Hiroi, T. K. Todorov, O. Gunawan, M. Kuwahara, T. Gokmen, D. Nair, M. Hopstaken, B. Shin, Y. S. Lee, W. Wang, H. Sugimoto and D. B. Mitzi, *Adv. Mater.*, 2014, **26**, 7427–7431.

9 I. Repins, N. Vora, C. Beall, S.-H. Wei, Y. Yan, M. Romero, G. Teeter, H. Du, B. To, M. Young and R. Noufi, *MRS Proc.*, 2011, **1324**, d17-1–12.

10 O. Gunawan, T. K. Todorov and D. B. Mitzi, *Appl. Phys. Lett.*, 2010, **97**, 233506-1–3.

11 P. Zawadzki, A. Zakutayev and S. Lany, *Phys. Rev. Appl.*, 2015, **3**, 34007.

12 S. Chen, A. Walsh, X.-G. Gong and S.-H. Wei, *Adv. Mater.*, 2013, **25**, 1522–1539.

13 D. Tiwari, T. Koehler, X. Lin, R. Harniman, I. Griffiths, L. Wang, D. Cherns, R. Klenk and D. J. Fermin, *Chem. Mater.*, 2016, **28**, 4991–4997.

14 C. M. Fella, Y. E. Romanyuk and A. N. Tiwari, *Sol. Energy Mater. Sol. Cells*, 2013, **119**, 276–277.

15 D. Tiwari, T. Koehler, X. Lin, A. Sarua, R. Harniman, L. Wang, R. Klenk and D. J. Fermin, *ACS Appl. Mater. Interfaces*, 2017, **9**, 2301–2308.

16 J. Rodríguez-Carvajal, *Phys. B Condens. Matter*, 1993, **192**, 55–69.

17 D. M. Berg, M. Arasimowicz, R. Djemour, L. Gutay, S. Siebentritt, S. Schorr, X. Fontane, V. Izquierdo-Roca, A. Perez-Rodriguez and P. J. Dale, *Thin Solid Films*, 2014, **569**, 113–123.

18 M. Dimitrievska, H. Xie, A. Fairbrother, X. Fontané, G. Gurieva, E. Saucedo, A. Pérez-Rodríguez, S. Schorr and V. Izquierdo-Roca, *Appl. Phys. Lett.*, 2014, **105**, 31913-1–5.

19 W. Sun, X. Geng, J. C. Armstrong, J. Cui and T. Chen, *2014 IEEE 40th Photovolt. Spec. Conf.*, 2014, 0421–0424.

20 A. P. Levanyuk and V. V. Osipov, *Sov. Phys. Uspekhi*, 1981, **24**, 187–215.

21 J. P. Teixeira, R. A. Sousa, M. G. Sousa, A. F. Da Cunha, P. A. Fernandes, P. M. P. Salome and J. P. Leitao, *Phys. Rev. B - Condens. Matter Mater. Phys.*, 2014, **90**, 235202-1–10.

22 J. Krustok, R. Josepson, M. Danilson and D. Meissner, *Sol. Energy*, 2010, **84**, 379–383.

23 J. Márquez-Prieto, M. V. Yakushev, I. Forbes, J. Krustok, P. R. Edwards, V. D. Zhivulko, O. M. Borodavchenko, A. V. Mudryi, M. Dimitrievska, V. Izquerdo-Roca, N. M. Pearsall and R. W. Martin, *Sol. Energy Mater. Sol. Cells*, 2016, **152**, 42–50.

24 E. Kask, M. Grossberg, R. Josepson, P. Salu, K. Timmo and J. Krustok, *Mater. Sci. Semicond. Process.*, 2013, **16**, 992–996.

25 S. Levcenko, J. Just, A. Redinger, G. Larramona, S. Bourdais, G. Dennler, A. Jacob and T. Unold, *Phys. Rev. Appl.*, 2016, **5**, 24004-1–10.

26 M. Grossberg, J. Krustok, K. Timmo and M. Altosaar, *Thin Solid Films*, 2009, **517**, 2489–2492.

27 M. Grossberg, J. Krustok, J. Raudoja, K. Timmo, M. Altosaar and T. Raadik, *Thin Solid Films*, 2011, **519**, 7403–7406.

28 J. Krustok, H. Collan, M. Yakushev and K. Hjelt, *Phys. Scr.*, 1999, **T79**, 179–182.

29 E. Zacks and A. Halperin, *Phys. Rev. B*, 1972, **6**, 3072–3075.

30 S. Schorr, *Sol. Energy Mater. Sol. Cells*, 2011, **95**, 1482–1488.

31 S. Chen, L. W. Wang, A. Walsh, X. G. Gong and S. H. Wei, *Appl. Phys. Lett.*, 2012, **101**, 223901-1–5.

32 S. Chen, X. G. Gong, A. Walsh and S. H. Wei, *Appl. Phys. Lett.*, 2010, **96**, 21902-1–4.

33 T. Walter, R. Herberholz, C. Müller and H. W. Schock, *J. Appl. Phys.*, 1996, **80**, 4411–4420.

34 P. A. Fernandes, A. F. Sartori, P. M. P. Salome, J. Malaquias, A. F. Da Cunha, M. P. F. Gracia and J. C. Gonzalez, *Appl. Phys. Lett.*, 2012, **100**, 233504.

35 Y. Y. Proskuryakov, K. Durose, B. M. Taele and S. Oelting, *J. Appl. Phys.*, 2007, **102**, 24504-1–11.

36 D. Tiwari, T. Koehler, R. Klenk and D. J. Fermin, *Sustain.*

Energy Fuels, 2017, **1**, 899–906.
37 J. T. Heath, J. D. Cohen and W. N. Shafarman, *J. Appl. Phys.*, 2004, **95**, 1000–1010.
38 K. Sardashti, E. Chagarov, P. D. Antunez, T. S. Gershon, S. T. Ueda, T. Gokmen, D. Bishop, R. Haight and A. C. Kummel, 2017, **9**, 17024–17033.
39 K. Yu and E. A. Carter, *Chem. Mater.*, 2016, **28**, 864–869.
40 D. M. Tobbens, G. Gurieva, S. Levcenko, T. Unold and S. Schorr, *Phys. Status Solidi Basic Res.*, 2016, **253**, 1890–1897.
41 J. J. S. Scragg, J. K. Larsen, M. Kumar, C. Persson, J. Sendler, S. Siebentritt and C. Platzer Björkman, *Phys. Status Solidi Basic Res.*, 2016, **253**, 247–254.
42 J. V. Li, D. Kuciauskas, M. R. Young and I. L. Repins, *Appl. Phys. Lett.*, 2013, **102**, 163905-1–4.
43 N. A. Kattan, I. J. Griffiths, D. Cherns and D. J. Fermín, *Nanoscale*, 2016, **8**, 14369–14373.